MODELLING OF CONCRETE FRACTURE AT AGGREGATE LEVEL USING DEM BASED ON X-RAY μCT IMAGES OF INTERNAL STRUCTURE

Key words: DEM, Concrete, Interfacial Transitional Zones, X-ray computed tomography.

Abstract. The paper describes two-dimensional meso-scale numerical results of fracture in notched concrete beams under quasi-static three-point bending. Concrete was modelled as a random heterogeneous 4-phase material composed of aggregate particles, cement matrix, interfacial transitional zones (ITZs) and air voids. As a numerical approach, the discrete element method (DEM) was used. The concrete micro-structure in calculations was directly taken from real concrete specimens based on 3D x-ray micro-computed tomography images and 2D images by the scanning electron microscope (SEM). Attention was paid to the shape of a fracture zone between aggregate grains. In addition, the effect of properties of ITZs on fracture was studied.

1   INTRODUCTION

Fracture is a fundamental phenomenon in concrete material [1-3]. It is very complex since it consists of main cracks with various branches, secondary cracks and micro-cracks [1]. During fracture, micro-cracks first arise in a hardening region on the stress-strain curve which change gradually during material softening into dominant distinct macroscopic cracks up to damage. The fracture process strongly depends upon a heterogeneous structure of materials over many different length scales, changing e.g. in concrete from the few nanometres (hydrated cement) to the millimetres (aggregate particles). In order to properly describe fracture in detail, material micro-structure has to be taken into account since its effect on the global results is pronounced [3]. The understanding of a fracture process is of major importance to ensure the safety of the structure and to optimize the material behaviour.

At the meso-scale, concrete may be considered as a composite material wherein four important phases may be separated: cement matrix, aggregate, interfacial transition zones ITZs and macro-voids [2,4,5]. In particular, the presence of aggregate and ITZs is important since the volume fraction of aggregate can be as high as 70-75% in concrete and ITZs with the thickness of about 50 µm are always the weakest regions in usual concretes [2], wherein cracking starts (because of their higher porosity). ITZs are a porous region of the cement paste around aggregate particles which is perturbed by their presence [6-8]. Their origin lies in the packing of the cement grains against the much larger aggregate which leads to a local increase in porosity (micro-voids) and a presence of small cement particles. A paste with the lower *w/c*

(higher packing density) or made from finer cement particles leads to ITZ of a smaller extent. This layer is highly heterogeneous and damaged and thus critical for the concrete behaviour. According to [8], two different types of failure exist for ITZs: the ITZ-aggregate separation (related to some delamination processes directly at the aggregate surface) and the ITZ-failure (related to cracking). The accurate understanding of the properties and behaviour of ITZ is one of the most important issues in the meso-scale analyses because damage is initiated in the weakest region and ITZ is just this weakest link in concrete.

The concrete behaviour at the meso-scale may be described with discrete models [2,9,10]. Within discrete methods, the most popular ones are: the classical particle discrete element method (DEM) [9-13], interface element models with constitutive laws based on non-linear fracture mechanics [14,15] and lattice methods [2,10,16-18]. In the models, the position and shape of inclusions was assumed to be random. The improved two-dimensional (2D) meso-scale fracture modelling results during uniaxial tension for 3-phase concrete based on x-ray computed tomography images was demonstrated by Ren et al. 2015 [19] using cohesive elements with a traction–separation law. The advantage of meso-scale modelling is the fact that it directly simulates micro-structure and can be used to comprehensively study local phenomena at the micro-level such as the mechanism of the initiation, growth and formation of localized zones and cracks which affect the macroscopic concrete behaviour (the concrete behaviour at the meso-scale fully determines the macroscopic non-linear behaviour). The mesoscopic results allow also for a better calibration of continuous and discontinuous constitutive continuum models and an optimization design of concrete with enhanced both strength and ductility [3,13]. Discrete models (if they are enough consistent) might progressively replace experimental tests to study the influence of concrete meso-structure (aggregates size, aggregate shape, aggregate roughness, aggregate/mortar volume, macro porosity, etc.) on the concrete behaviour. The disadvantages are: enormous computational cost and a difficult calibration procedure with respect to geometric and mechanical properties of ITZs.

The main objective of this study is to investigate a complicated fracture process 2D conditions in concrete elements under bending at aggregate level discrete model (based on DEM). The concrete heterogeneity was characterised by four phases, namely, aggregate grains, cement matrix, ITZs and air voids. The geometry of concrete micro-structure was directly taken from real concrete specimens using 2 high resolution and non-destructive techniques, i.e. 3D x-ray micro-computed tomography and 2D scanning electron microscope (SEM). Calculations were performed with the three-dimensional spherical discrete element model YADE, which was developed at University of Grenoble [20-21]. The model was successfully used for describing the behaviour of different engineering materials with a granular structure (mainly of granular materials by taking shear localization into account [22]). It demonstrated also its usefulness to fracture simulations in concrete [13]. The numerical outcomes were directly compared with the experimental results with respect to force-deflection curves and crack patterns.

The major contribution of the paper are calculation results on concrete fracture under bending by meso-scale model, wherein concrete was modelled as the 4-phase material with angularly-shaped aggregate particles. The calculated results were directly compared with the experimental images from an in-situ micro-scale x-ray micro-tomograph test. In the first step, 2D calculations were carried out only in order to check the capability of method. Attention

was laid on the crack shape propagating between aggregate particles and the effect of ITZs on the macroscopic concrete response with respect to the strength and crack formation.

2 EXPERIMENTAL RESULTS

The concrete was prepared from the ordinary Portland cement (CEM I 32.5 R), aggregate and water. The mean aggregate diameter was d_{50}=2 mm, maximum aggregate diameter d_{max}=16 mm and aggregate volume V_{agg}=75%.

The tests were carried out on 2 free-supported rectangular notched concrete beams (height H=80 mm, depth B=40 mm and length L=320 mm) (Fig. 1). The notch of the height of $H/10$=8 mm and width of 3 mm was located in the beam mid-span. The average uniaxial compressive strength f_c measured on the concrete specimens $10\times10\times10$ cm^3, Young's modulus E and Poisson's ratio υ measured on the concrete specimens 15×30 cm^2 were equal to: f_c=51.81 MPa, E=36.1 GPa and υ=0.22 respectively. The measured tensile strength during bending on the concrete beams $4\times4\times16$ cm^2 was f_t=3.7-4.3 MPa. The quasi-static beam tests were performed with a controlled notch opening displacement rate (crack mouth opening displacement (CMOD)) of 0.002 mm/min using the loading machine Instron 5569. The CMOD gauge with the length of 5 mm was located in the notch at the beam bottom. Its accuracy was 0.0025 mm for the maximum permissible axial displacement of 2 mm. The test ended for CMOD=0.10-0.15 mm.
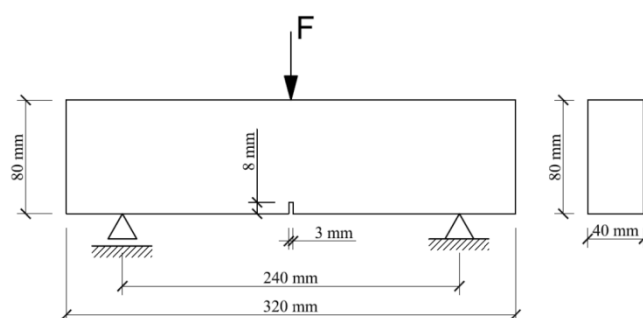

Figure 1: Concrete notched beam under quasi-static three-point bending: geometry and boundary conditions of beam (F -vertical force)

Figure 2 demonstrates the 3D images of the cracked cubical concrete specimens $80\times50\times40$ mm^3 (height×width×depth) which were cut out from the beams in the notch region after each test. The specimen of Fig.2a was cut out from the beam '1' for CMOD≈0.15 mm (when the beam was totally cracked along its height) and the specimen of Fig.2b comes from the beam '2' for CMOD=0.10 mm.

The total volume of air voids was 5.02% (specimen '1') and 4.67% (specimen '2'). In order to examine the crack variation in performance with micro-structural heterogeneity, the results for 3 various vertical cross-sections of the concrete cuboids after the tests are presented in Fig.3 (for CMOD=0.15 mm - beam '1' and CMOD=0.10 mm - beam '2').

The main crack was strongly curved mainly due to presence of aggregate grains (Fig. 2). Its shape changed along the specimen depth in spite of the fact that 2D boundary value problem (plane stress) was considered. The crack mainly propagated through ITZs (which

were the weakest phase in concrete) and sometimes through macro-voids (Fig. 4a). It might very rarely propagate through a single weak aggregate particle (Fig.4b). The crack branching also occurred (Fig.4c). The effect of air macro-voids on the crack shape was small.
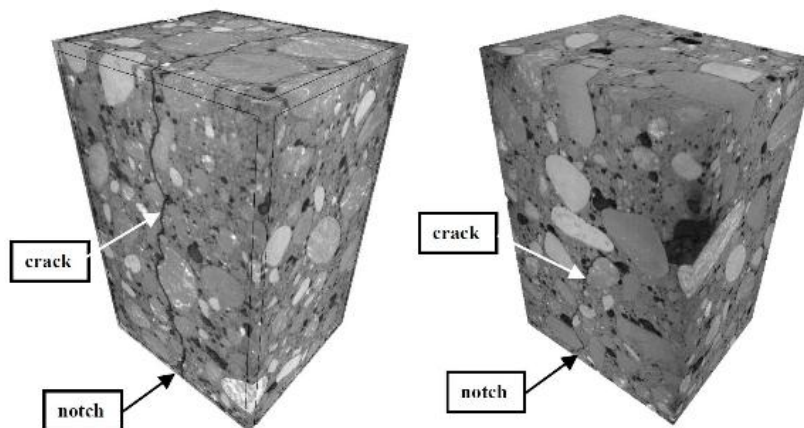

Figure 2: Images of cracked cuboidal specimens 50x50x40 mm³ obtained by 3D micro-CT cut out from: a) beam '1' and b) beam '2' (black spots – voids)
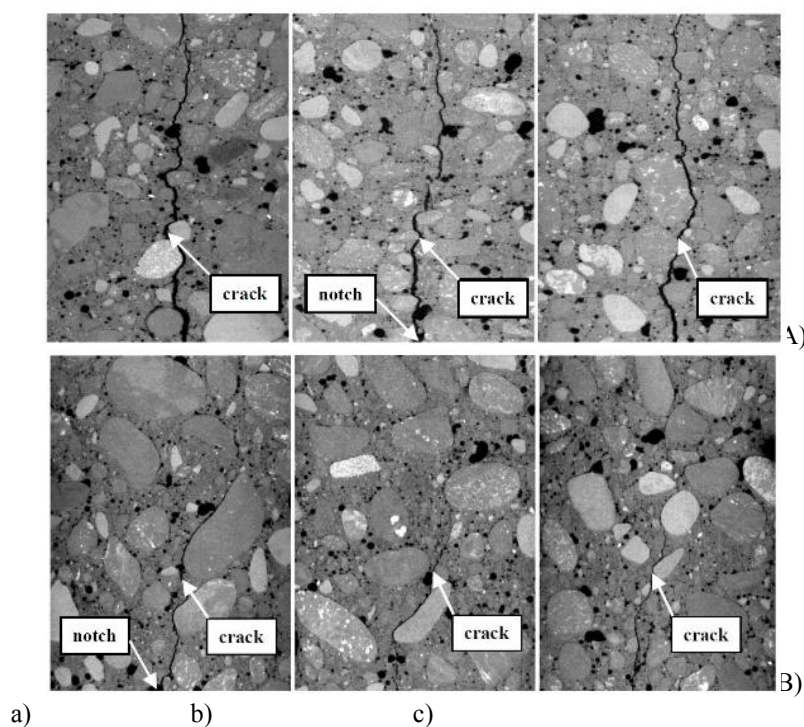

Figure 3: Crack shape in cuboidal concrete speciments 80×50×40 mm³ of A) Fig.2a and B) Fig.2b after test based on 3D μCT images in 3 different vertical cross-sections: a) at depth of 3 mm, b) at depth of 20 mm (mid-region) and c) at depth 37 mm from front beam surface (black spots denote voids)

The crack width changed non-linearly with the specimen height from w_c=0.75 mm (just above the notch) down to w_c=0.22 mm (top) (mid-cross-section of the specimen '1') and from

w_c=0.32 mm (just above the notch) down to w_c=0.02 mm (top) (mid-cross-section of the specimen '2'). The crack width above the notch varied with the specimen depth from w_c=0.45 mm (at the depth of 10 mm from the face side) up to w_c=0.75 mm (the mid-sectional cross-section) (specimen '1') and from w_c=0.32 mm (at the depth of 5 mm from the face side) down to w_c=0.13 mm (at the depth of 35 mm) (specimen '2'). The average crack width in the specimen '1' was w_c=0.41 mm wherein the crack propagated through the specimen. In the specimen '2', the average crack width and height were: w_c=0.20 mm and h_c=50 mm, respectively. The crack height in the specimen '2' changed along the specimen depth, from h_c=45 mm up to h_c=56 mm on the front specimen side. The width of the localized zone above the notch on the beam surface, measured by DIC, was w_{lz}=3.11-3.40 mm [23].

In order to measure the width of ITZs, the scanning electron microscope (SEM) Hitachi TM3030 with the maximum magnification factor 30'000 was used. ITZs around aggregate particles were characterised by a very non-uniform porous structure and presence of separated small sand particles. ITZs appeared mainly aggregate particles but sometimes they were also visible around larger cement matrix particles. The width of ITZs changed between 30-50 μm (Fig. 5). The width was not dependent upon the aggregate diameter.
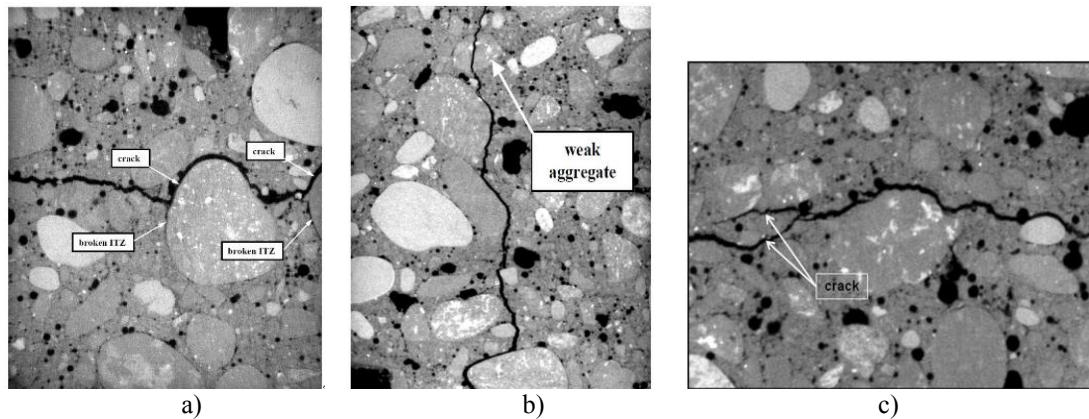

a)   b)   c)

Figure 4: Crack propagation a) in ITZ b) throught single aggregate and c) crack branching in experiments based on 3D μCT images (beam '1') (black spots denote voids)
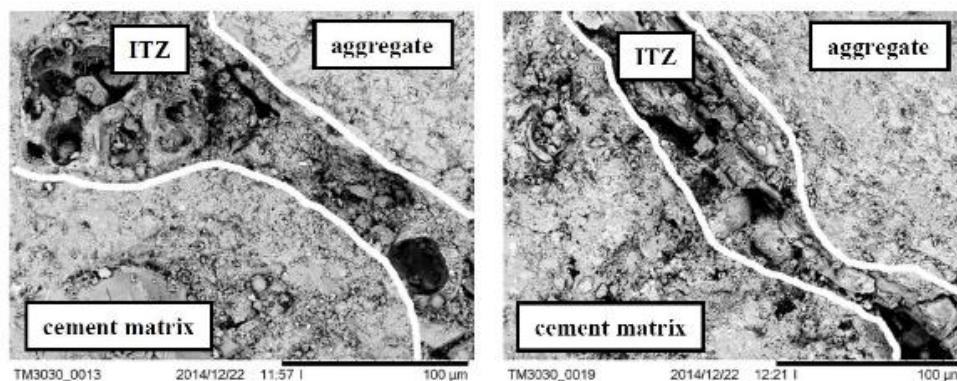

Figure 5: Scanning electron micrographs of ITZ around aggregate particles in concrete specimen '1' (magnification factor 1'000)

3 DISCRETE ELEMENT METHOD FOR CONCRETE

The 3D spherical discrete element model YADE takes advantage of the so-called soft-particle approach (i.e. the model allows for particle deformation which is modelled as an overlap of particles) [31-32]. A linear normal contact model under compression was used. Aggregate grains were modelled as clusters composed of spheres. The interaction force vector representing the action between two spherical discrete elements in contact was decomposed into a normal and tangential vector, respectively. The normal forces acting on spheres were modelled by an elastic law with cohesion. The normal and tangential forces were linked to the displacements through the normal stiffness K_n and the tangential stiffness K_s (Figs. a-6c) [21]

$$(1)$$

$$(2)$$

where U is the overlap between spheres, $\vec{N}$ denotes the normal vector at the contact point, $\Delta\vec{X}$ is the incremental tangential displacement and $\vec{F}_{s,prev}$ is the tangential force from the previous iteration.

The stiffness parameters were computed with the aid of the modulus of elasticity of the grain contact E_c and two neighbouring grain radii R_A and R_B (to determine the normal stiffness K_n) and with the aid of the modulus of elasticity E_c and Poisson's ratio v_c of the grain contact and two neighbouring grain radii R_A and R_B (to determine the tangential stiffness K_s), respectively [21]. The contact forces $\vec{F}_s$ and $\vec{F}_n$ satisfied the cohesive-frictional Mohr-Coulomb equation (Fig. 6d)

$$(before\ contact\ breakage) \qquad (3)$$

and

$$(after\ contact\ breakage) \qquad (4)$$

where μ denotes the inter-particle friction angle and   is the cohesive force between spheres. The normal force might be negative down to the minimum value of   if there was no a geometrical contact between elements. If this minimum normal force between spheres   was reached, the contact was broken. Moreover, if any contacts between grains re-appeared, cohesion between them was not taken into account. A crack was considered as open if cohesive forces between grains disappeared when a critical threshold was reached. The movement of fragments (mass-spring systems with cohesion) was similar to the rigid body movement [32].

A choice of a very simple linear elastic normal contact was intended to capture on average various contact possibilities in real concrete. One assumed that the cohesive force and tensile force were a function of the cohesive stress C (maximum shear stress at pressure equal to zero), tensile normal stress T and sphere radius R [21]

$$and \qquad F_{min}^n = T \cdot R^2 \qquad (5)$$

For two elements in contact, the smaller values of C, T and R were assumed. To dissipate excessive kinetic energy in a discrete system, a simple local non-viscous damping scheme was adopted [24] which assumed a change of forces by using the damping parameter α:

$$|, \qquad (6)$$

where $\vec{F}^k$ and $\vec{v}^k$ are the kth components of the residual force and translational velocity, respectively. A positive damping parameter α is smaller than 1 (sgn(•) returns the sign of the

k^{th} component of velocity). The equation can be separately applied to each kth component of a 3D vector x, y and z.
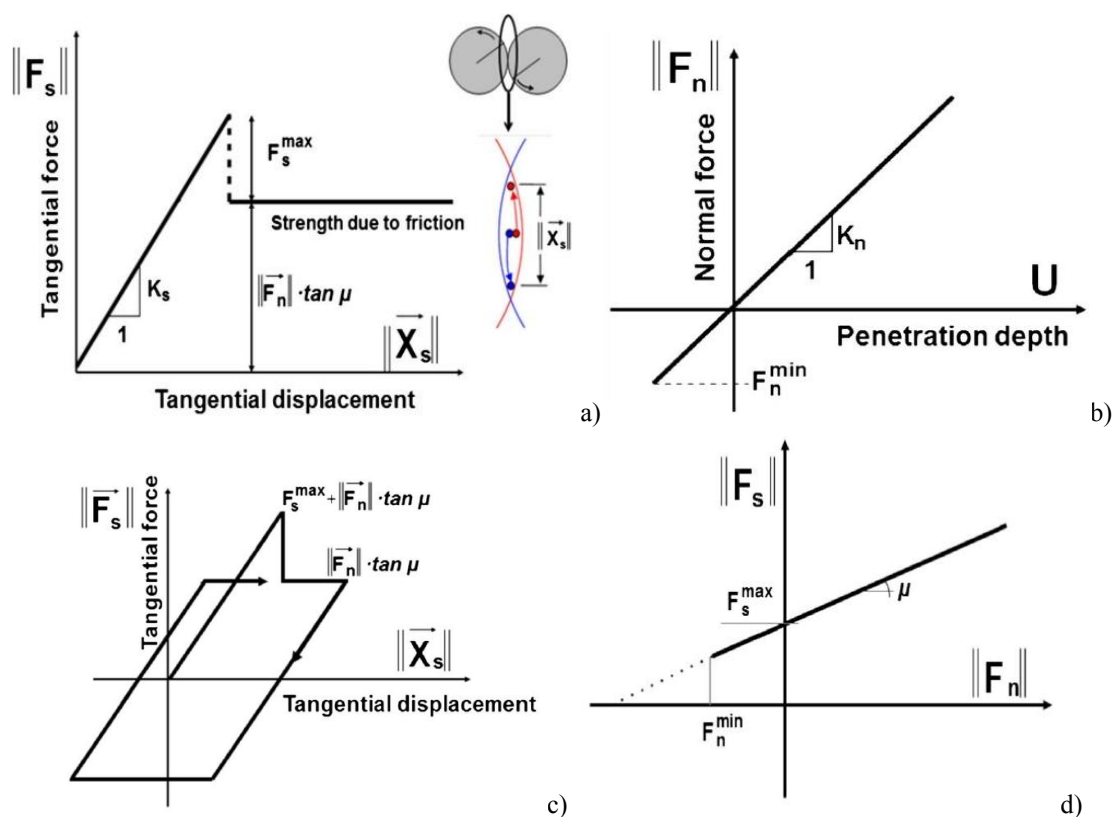

Figure 6: Mechanical response of DEM: a) tangential contact model, b) normal contact model, c) loading and unloading path in tangential contact model and d) modified Mohr-Coulomb model [20], [21]

The following 5 main local material parameters were needed for our discrete simulations: E, υ, μ, C and T which may be successfully calibrated with real laboratory uniaxial tests on compression and tension of concrete specimens [13]. In addition, the particle radius R, particle mass density ρ and damping parameters α are required. Note that material softening was not directly assumed in the model.

In DEM computations of the concrete beam as a four-phase material, aggregates (d=2-16 mm) were modelled as grain clusters with the diameter of d=0.5 mm connected to each other as rigid bodies. One aggregate, depending upon its diameter, included 10-500 cylinders. All aggregate grains (d>2 mm) included ITZs. The aggregate volume was 75%. The cement matrix was modelled with the spheres with the diameter d=0.25-2 mm without ITZs. The cement matrix grains filled the concrete specimen in 95% [13]. The macro air voids (d>0.8 mm) where assumed as the empty spaces. The remaining beam region (outside the meso-region close to the notch) was simulated with the spheres of d=2-8 mm (Fig. 7a). In order to significantly shorten the computations, the beam included only one layer of grains [13] for 2D calculations. For the sake of simplicity, ITZs were solely simulated as the contacts between aggregate and cement matrix grains (thus they had a no physical width).
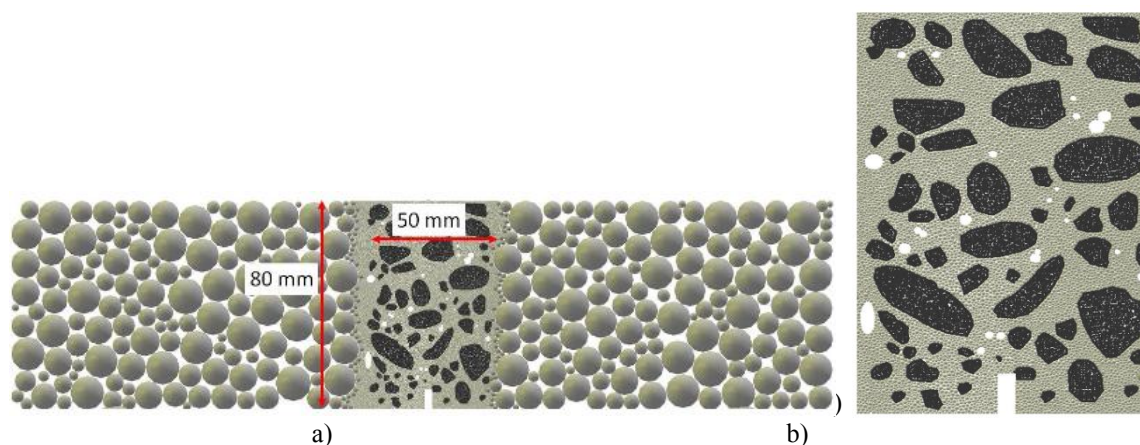
Figure 7: 2D DEM grain geometry for concrete beam '2': a) entire beam and b) meso-region close to notch of 50×80 mm^2 based on tomography image of Fig.2 (mid-sectional cross-section)(white spots denotes voids)

Based on preliminary calculations of uniaxial compression and uniaxial tension tests [13] biaxial compression tests, the following parameters of cohesion and tensile strength were assigned to the cement matrix ($E_{c,cm}$=29.2 GPa, C_{cm}=140 MPa and T_{cm}=25 MPa) and ITZs ($E_{c,ITZ}$=20.4 GPa, C_{ITZ}=100 MPa and T_{ITZ}=17.5 MPa). Note that there were no contacts between aggregate grains. In the remaining region outside the meso-region with large grains was described by the constants: E_{macro}=36.1 GPa, C_{macro}=140 MPa and T_{macro}=25 MPa. The contact elastic stiffness of the cement matrix and beam macro-zone of Fig. 9a were taken directly from laboratory tests. The remaining material parameters were constant for all phases and regions: υ_c=0.2 (Poisson's ratio of grain contact), μ=18° (inter-particle friction angle), α_d=0.08 (damping parameter) and ρ=2.6 kG/m^3 (mass density). The inter-particle friction angle was assumed based on triaxial compression tests with granulates in the form of clumps [28]. The material constants C i T were adopted with the aid of the uniaxial compression test (2D concrete specimen 10×10 cm^2) and bending test (2D concrete specimen 4×16 cm^2) with concrete (Section 2) through a comparison between experiments and numerical outcomes [13]. With the assumed material properties and grain size distribution curve, the DEM calculations provided the uniaxial compressive strength of 49.5 MPa, the compressive elastic modulus of 36 GPa and the tensile strength during bending of 4.40 MPa (2D concrete specimen 4×16 cm^2), i.e. similarly as in the experiments of Section 2 (f_c=51.81 MPa, f_t=4.04 MPa, E=36.1 GPa and f_t=3.7-4.3 MPa).

The beam included in total about 25'000 grains (20'000 grains in the meso-region with d_{min}=0.25 mm) (Fig. 7). Each concrete beam was constructed in a simple way by putting grain clusters in the position of aggregate in the beam meso-region. Next the cement matrix grains were randomly added to the meso-region with the inter-granular friction angle equal to μ=0° in order to obtain a relatively dense specimen. The beam macro-region was filled up with the spheres of the beam of d=2-8 mm with μ=0°. The entire assembly was then allowed to settle to a state when the kinetic energy was negligible and then all contact forces between spheres were deleted. In the places where macro air voids existed, the grains were deleted. Before the beam was loaded, the final parameters C, T and μ were imposed. Afterwards the element assembly was subjected to deformation. The constant vertical velocity v=2 mm/s was applied

at the place of *F*. The imposed damping factor and the velocity of the prescribed displacement did not affect the results [13]. The calculated nominal inertial number *I* (which quantifies the significance of dynamic effects) was $<10^{-3}$ that usually corresponded to a quasi-static regime.

4   NUMERICAL RESULTS

Figures 10 demonstrate the force-CMOD curves obtained for the concrete beams '1' and '2' with the real aggregate and air voids distribution in three different cross-sections of Figs. 3A and 3B in the notch region using. The calculated maximum vertical force was *F*=2.11-2.21 kN for CMOD=0.014-0.015 mm (beam '1') and *F*=2.22-2.70 kN for CMOD=0.015-0.016 mm (beam '2') (Fig. 8). The peaks were similar like in experimental (except beam '2' mid-section where peak was higher 20%). The calculated residual forces were similar in the beam '1' and higher by 20-100% in the beam '2'. The calculated forces versus CMOD indicated clear fluctuations after the peak (smaller d_{min} or 3D calculations should solve this fluctuations).

The shape of the crack in DEM was also similar as in the experiments; the crack propagated mainly through ITZs and sometimes by macro air voids (Figs.9 and 10). The maximum calculated length and height of the crack above the notch (beam '2') were: l_{lz}=59.6-63.0 mm and h_{lz}=51.3-53.1 mm (h_{lz}/H≈0.71-0.74). However, some differences with respect to the propagation way appeared. In the mid-section of the beam '2' (Fig. 10B), the way of the calculated crack was different from the same beginning. Sometimes the calculated crack run around the different side of small aggregate particles. One also could observe clear crack branches in some points (e.g. in the beam '2', Figs.10B and 10C), similarly as in the experiments (Fig. 4c). Some single contacts also broke down away from the main crack.
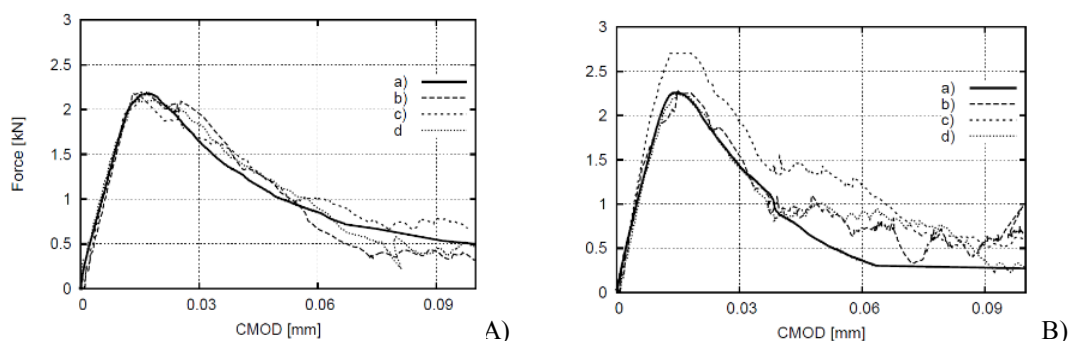

Figure 8: Evolution of vertical force against CMOD from numericla calculations: a) experimental curves of Fig.3, b-d) calculated curves for concrete micro - structure of Fig.6A and 6B (beam '1' (A) and beam '2' (B))

In Fig. 11a, the evolution of the broken contacts in DEM is shown. The total number of contact decreased from 35'380 (for CMOD=0.015 mm – the point of the maximum vertical force) down to 33'300 (CMOD=0.06-0.10 mm). A large number of interfacial micro-cracks initiated very quickly at an early stage of loading (their growth was stable). The largest non-uniform development of micro-cracks took place when CMOD≈0.019 mm (slightly after the peak load). From CMOD>0.06 mm, the breakage was negligible. Some sudden drops in the broken contact number denoted the crack propagation in ITZs (the weakest phase); the mild

drops denoted the crack propagation in the cement matrix. Some secondary cracks beyond the main crack could also close. The width of the damage zone (corresponding to the broken contacts) was about 1.5-2 mm (Fig. 11b). The width of fully open cracks was about 0.15-0.29 mm (in experiments the crack width was slightly smaller 0.11-0.23 mm). The width of the localized zone above the notch (based on grain displacements) was w_{lz}=2.16-2.84 mm (beams '1' and '2') for CMOD=0.014 mm (above the beam notch). Its largest width was w_{lz}=3.44 mm (at the high of h=30 mm).
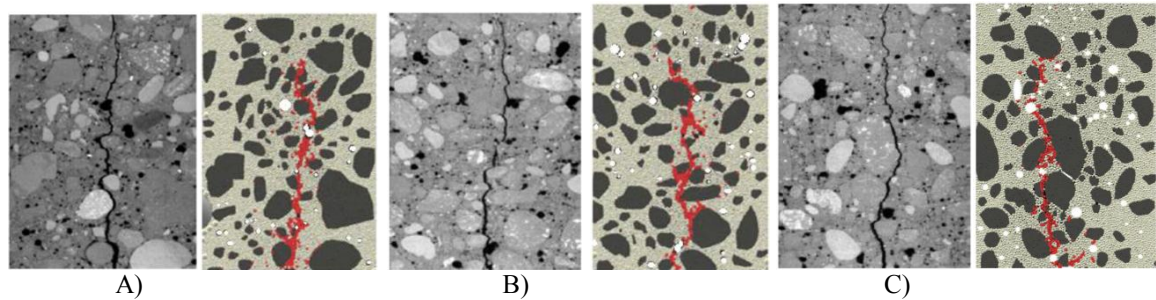

Figure 9: Fracture in concrete beam '1' above notch: left) experiments (images by micro-CT after test for CMOD=0.15 mm and right) breakage of contacts in DEM (CMOD=0.10 mm), A) at depth of 3 mm, B) at depth of 20 mm (mid-region) and C) at depth 37 mm from front beam surface of Fig.3A)
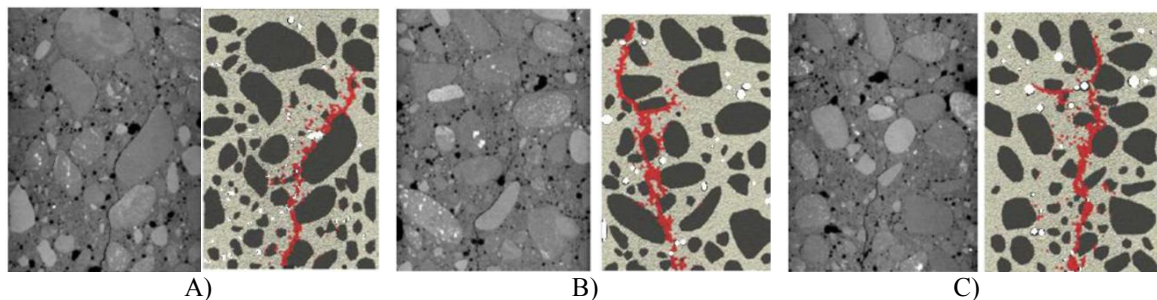

Figure 10: Fracture in concrete beam '2' above notch: left) experiments (images by micro-CT after test for CMOD=0.15 mm and right) breakage of contacts in DEM (CMOD=0.10 mm), A) at depth of 3 mm, B) at depth of 20 mm (mid-region) and C) at depth 37 mm from front beam surface of Fig.3B)

5 CONCLUSIONS

Discrete meso-scale model based on DEM were developed based on high-resolution x-ray micro-tomography images to simulate fracture processes in concrete beams under three-point bending. The calculation 2D results for four-phase concrete at aggregate level using a discrete element model showed satisfactory quantitative agreement with experimental observations.

The experimental crack above the notch was strongly curved and depended on concrete micro-structure. It mainly propagated through the weakest contact zones (ITZs) between the cement matrix and aggregates. The width of ITZs varied between 30 and 50 μm. Their porosity was strongly uniform. The crack might rarely propagate through a weak aggregate

particle. Some small crack branches were also visible. The crack shape was different with the beam depth.

It was found that the mechanical properties of ITZs had a pronounced influence on the material strength and macro-cracking that demonstrates the necessity of their experimental investigations, 3D modelling and small grain presence in DEM computations.
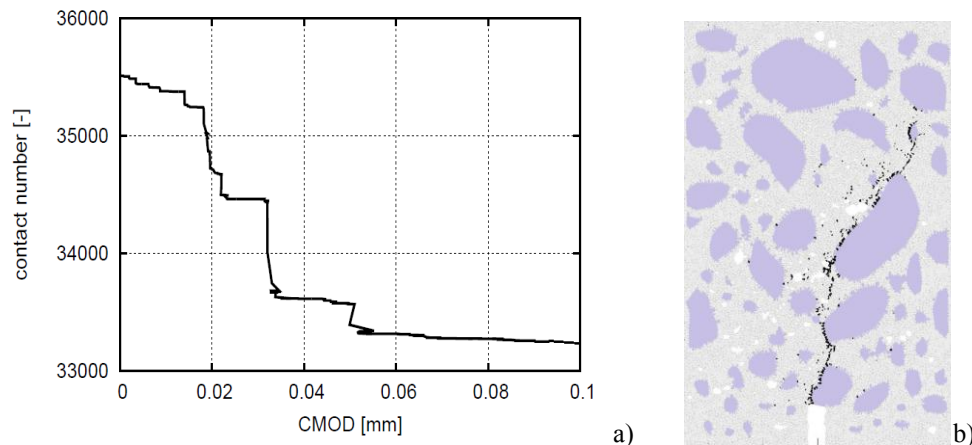

Figure 11: Broken contacts in concrete beam '2' at depth of 3 mm for DEM calculations a) evolution of contact number versus CMOD and b) broken contacts in notch region above for CMOD=0.1 mm (black lines)

Acknowledgements

REFERENCES

[1] Bažant, Z. and Planas, J. *Fracture and size effect in concrete and other quasi-brittle materials*. CRC Press LLC (1997), Boca Raton.

[2] Lilliu, G. and van Mier, J.G.M. 3D lattice type fracture model for concrete. *Engineering Fracture Mechanics* (2003) **70**:927-41.

[3] Tejchman, J. and Bobiński, J. *Continuous and discontinuous modelling of fracture in concrete using FEM*. Springer, Berlin-Heidelberg (2013)(eds. W. Wu and R. I. Borja).

[4] Skarżyński, Ł. and Tejchman, J. Calculations of fracture process zones on meso-scale in notched concrete beams subjected to three-point bending. *European Journal of Mechanics A/Solids* (2010) **29**:746-60.

[5] Skarżyński, Ł. and Tejchman, J. Modelling the effect of composition on the tensile properties of concrete. *Understanding the tensile properties of concrete* (ed. J. Weerheijm). Woodhead Publishing Limited (2013), 52-97.

[6] Scrivener, K.L., Crumbie, A.K. and Laugesen, P. The interfacial transition zone (ITZ) between cement paste and aggregate in concrete. *Interface Science* (2004) **12**:411-21.

[7] Mondal, P., Shah, S.P. and Marks, L.D. Nanomechanical properties of interfacial transition zone in concrete. *Nanotechnology in Construction* (2009) **3**:315-20.

[8] Königsberger, M., Pichler, B. and Hellmich, Ch. Micromechanics of ITZ-aggregate interaction in concrete Part II: strength upscaling. Journal of American Ceramic Society. *Journal of American Ceramic Society* (2014) **97**:543-51.

[9] Hentz, S., Daudeville, L. and Donze, F. Identification and validation of a Discrete Element Model for concrete. *Journal of Engineering Mechanics AS*CE (2004) **130**:709-19.

[10] Kozicki, J. and Tejchman, J. Modelling of fracture processes in concrete using a novel lattice model. *Granular Matter* (2008) **10**:377-88.

[11] Donze, F.V., Magnier, S.A., Daudeville, L. and Mariotti, C. Numerical study of compressive behaviour of concrete at high strain rates. *Journal for Engineering Mechanics* (1999) **122**:1154-63.

[12] Dupray, F., Malecot, Y., Daudeville, L. and Buzaud, E.A. mesoscopic model for the behaviour of concrete under high confinement. *I. J. Numerical and Analytical Methods in Geomechanics* (2009) **33**:1407-23.

[13] Nitka, M. and Tejchman, J. Modelling of concrete behaviour in uniaxial compression and tension with DEM. *Granular Matter* (2015) **17**:145-64.

[14] Carol I, López CM, Roa O. Micromechanical analysis of quasi-brittle materials using fracture-based interface elements. *I. J. Num. Methods in Engineering* (2001) **52**:193-215.

[15] Caballero, A., Carol, I. and López, C.M. New results in 3D meso-mechanical analysis of concrete specimens using interface elements, *Computational Modelling of Concrete Structures EURO-C* (eds.:G. Meschke, R. de Borst, H. Mang and N. Bićanić), Taylor and Francis Group (2006);43-52.

[16] Jirásek, M., Bažant, Z.P. Particle model for quasi-brittle fracture and application to sea ice. *Journal of Engineering Mechanics* (1995);**121**:1016-25.

[17] Schlangen, E. and Garboczi, E.J. Fracture simulations of concrete using lattice models: computational aspects. *Engineering Fracture Mechanics* (1997) **57**:319-32.

[18] Bolander, J.E. and Sukumar, N. Irregular lattice model for quasi-static crack propagation. *Physycial Review B* (2005) **71**:094106.

[19] Ren, W., Yang, Z., Sharma, R., Zhang, Ch. and Withers, P.J. Two-dimensional X-ray CT image based meso-scale fracture modelling of concrete. *Engineering Fracture Mechanics* (2015) **133**: 24-39.

[20] Kozicki, J. and Donze F. A new open-source software developer for numerical simulations using discrete modeling methods. *Computer Methods in Applied Mechanics and Engineering* (2008) **197**:4429-43.

[21] Šmilauer, V. and Chareyre, B. *Yade DEM Formulation*. Manual, (2011).

[22] Kozicki, J., Tejchman, J. and Műhlhaus, H.B. Discrete simulations of a triaxial compression test for sand by DEM. *I. J. Numerical and Analytical Methods in Geomechanics* (2014) **38**:1923-52.

[23] Skarżyński, Ł. and Tejchman, J. Experimental investigations of fracture process in plain and reinforced concrete beams under bending. *Strain* (2013) **49**:521-43.

[24] Cundall, P.A. and Hart, R. Numerical modelling of discontinua. *Engineering Computations* (1992) **9**:101-13.